ACS Catalysis

Research Article

pubs.acs.org/acscatalysis

Nitrogen and Phosphorus Dual-Doped Graphene/Carbon Nanosheets as Bifunctional Electrocatalysts for Oxygen Reduction and Evolution

Rong Li,[†,‡] Zidong Wei,[*,†] and Xinglong Gou[*,‡]

[†]The State Key Laboratory of Power Transmission Equipment and System Security and New Technology, College of Chemistry and Chemical Engineering, Chongqing University, Chongqing 400044, China

[‡]Chemical Synthesis and Pollution Control Key Laboratory of Sichuan Province, College of Chemistry and Chemical Engineering, China West Normal University, Nanchong 637000, China

Supporting Information

ABSTRACT: It is highly desirable but challenging to develop bifunctional catalysts for efficiently catalyzing both the oxygen reduction reaction (ORR) and oxygen evolution reaction (OER) in energy storage and conversion systems. Here a simple yet cost-effective strategy is developed to fabricate nitrogen and phosphorus dual-doped graphene/carbon nanosheets (N,P-GCNS) with N,P-doped carbon sandwiching few-layers-thick graphene. The as-prepared N,P-GCNS shows outstanding catalytic activity toward both ORR and OER with a potential gap of 0.71 V between the OER potential at a current density of 10 mA cm^{-2} and the ORR potential at a current density of −3 mA cm^{-2}, illustrating that it is the best metal-free bifunctional electrocatalysts reported to date. The superb bifunctional catalytic performance is attributed to the synergistic effects between the doped N and P atoms, the full exposure of the active sites on the surface of the N,P-GCNS nanosheets, the high conductivity of the incorporated graphene, and the large surface area and hierarchical pores for sufficient contact and rapid transportation of the reactants.

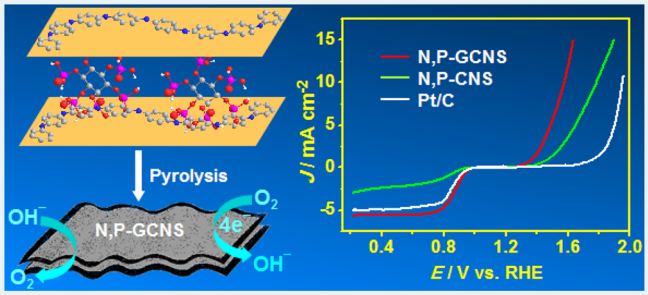

KEYWORDS: *electrocatalysis, oxygen reduction reaction, oxygen evolution reaction, graphene, heteroatom doping*

1. INTRODUCTION

Oxygen reduction reaction (ORR) and oxygen evolution reaction (OER) are the key electrode processes for a variety of sustainable energy technologies such as metal−air batteries, regenerative fuel cells, water splitting, and solar fuel synthesis.[1] Nevertheless, both ORR and OER processes suffer from sluggish kinetics, and thus electrocatalysts are critical in these fields.[2] At present, the best catalysts for ORR or OER consist of platinum-group metals, which are scarce and expensive. Furthermore, good catalysts for ORR often exhibit poor activity toward OER and vice versa.[3] Therefore, it is highly desirable but challenging to develop affordable and efficient bifunctional electrocatalysts for both ORR and OER.[4]

Recently, nonprecious transition metal oxides and chalcogenides have been reported to show catalytic activity toward both ORR and OER.[5] However, their catalytic potency is impaired by their poor electronic conductivity. Meanwhile, metal-free carbonaceous materials doped with heteroatoms (e.g., N, P, B, S, or I) have been the focus of oxygen electrocatalysis since the first report on nitrogen-doped carbon nanotube arrays with better ORR catalytic activity than commercial Pt/C catalyst.[6,7] Both theoretical calculations and detailed experiments have revealed that the high ORR activity of doped carbon materials is attributed to the abundant active sites created by heteroatom doping, which induce changes in the local charge density and asymmetry spin density of the carbon lattice.[6a,8] Lately, N-doped carbon nanomaterials have also been demonstrated to be potential alternatives to transition metal-based OER catalysts,[9] suggesting their potential as bifunctional electrocatalysts. Most recently, N-doped graphene (NG),[10] NG/carbon nanotube hybrid (NG/CNT),[11] and N-doped coaxial carbon nanocables (CNT@NCNT)[12] have been found to be active for both ORR and OER. However, their performance as bifunctional oxygen electrocatalysts was still limited by either small surface area or low level of nitrogen doping, both of which determine the available active sites and catalytic activity of the electrocatalysts. In addition, recent studies show that codoping carbons with nitrogen and other heteroatoms can significantly improve their ORR performance owing to the increased number of dopant heteroatoms and the synergistic effects between the doped heteroatoms.[13] Inspired by these finds, we conjecture that binary or multiple-element-doped nanocarbons could provide further space for performance optimization of the metal-free

Received: March 20, 2015
Revised: May 8, 2015
Published: May 27, 2015

DOI: 10.1021/acscatal.5b00601
ACS Catal. 2015, 5, 4133−4142

Scheme 1. Schematic Illustration of the Fabrication Process and Structure of the N,P-GCNS Bifunctional Oxygen Electrocatalyst

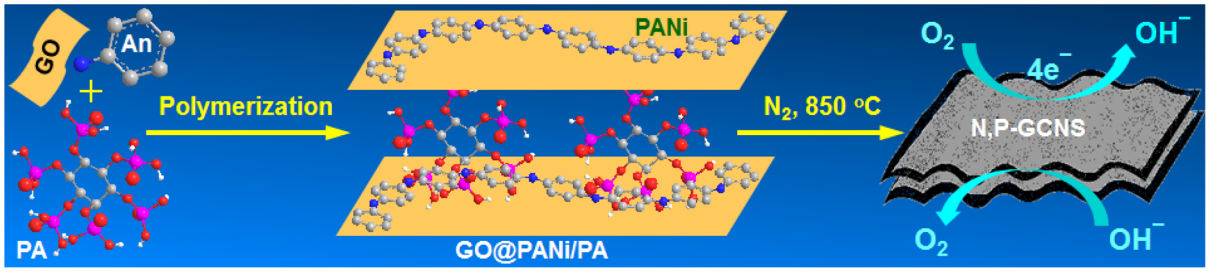

bifunctional oxygen electrocatalysts. Nevertheless, rare successful cases have been reported in this field.[14]

Herein, we present a facile yet cost-effective strategy to fabricate nitrogen and phosphorus dual-doped graphene/carbon nanosheets (N,P-GCNS) by pyrolysis of a dried hydrogel composed of graphene oxide (GO), polyaniline (PANi), and phytic acid (known as inositol hexaphosphoric acid, PA) as depicted in Scheme 1, where GO nanosheets were employed as the precursor of graphene and the structure directing agents for conformal coating of PANi and PA molecules during polymerization of aniline (An) monomers. As a proof of concept, the as-prepared N,P-GCNS can be used as a novel metal-free bifunctional electrocatalyst in reversibly catalyzing oxygen reduction and evolution reactions with much better catalytic performance not only than the corresponding single-heteroatom-doped counterpart but also than most of the reported metal-based electrocatalysts thanks to synergetic effects of the doped N and P atoms, high active surface area, good conductivity, and unique porous structure for transportation of both gas and electrolyte.

2. EXPERIMENTAL SECTION

2.1. Materials Preparation. GO powders was prepared according to the modified Hummer's method as described elsewhere.[15] N,P-GCNS were synthesized through direct pyrolysis of GO sheets conformally coated with a layer of PANi and PA. Typically, An (0.46 mL) in alcohol (2 mL) was dropped into GO dispersion (30 mL, 2 mg mL^{-1}) under continuous stirring. Then, an aqueous solution (3 mL) containing PA (0.92 mL) and ammonium peroxydisulfate (APS, 0.29 g) was added dropwise into the above mixture in an ice bath under vigorous stirring. A gel was formed after 24 h of stirring, and it was directly dried in a rotary evaporation. Finally, the mixture was heated at 850 °C for 2 h under nitrogen flow. For comparison, N,P-doped carbon nanospheres (N,P-CNS, without graphene) were fabricated through the same procedure except without addition of GO. N-doped carbon nanoparticles (N-CNP, without P and graphene) were also prepared by pyrolysis of pristine PANi obtained by using hydrochloride acid instead of PA as the catalyst to exclude P-doping in the final product. N-doped graphene (N-G, without P) was prepared through the same procedure of N-CNP in the presence of GO during polymerization. P-doped graphene (P-G, without N) was obtained by pyrolyzing the dried mixture of PA−GO.

2.2. Structural Characterization. The morphology and microstructure were observed by field emission scanning electron microscope (FESEM, Hitachi S-4800) and transmission electron microscope (TEM, FEI Tecnai F20). X-ray diffraction (XRD) patterns were recorded on an XRD diffractometer (Rigaku Ultima IV, Cu Kα radiation). Raman spectra were collected on a Micro-Raman spectroscopy system (Renishaw inVia-reflex, 532 nm excitation laser). The surface chemical composition was determined by X-ray photoelectron spectroscopy (XPS, Shimazu-Kratos AXIS UTLTRA DLD) using a monochromated Al Kα source. The surface area and pore structure were characterized on an automated gas sorption analyzer (Autosorb-iQ, Quantachrome) with N_2 as adsorbate. The specific surface areas of the samples were determined from the nitrogen adsorption/desorption isotherms by using the Brunauer−Emmett−Teller (BET), whereas the pore size distribution curves were derived from the Barrett−Joyner−Halenda (BJH) method (for mesopores) and the density functional theory (DFT) approach (for micropores).

2.3. Electrochemical Tests. All electrochemical measurements were conducted at room temperature on a computer-controlled bipotentiostat (CHI 760E, CH Instrument, Shanghai, China) assembled with a rotational system (Pine Research Instrumentation, Durham, NC, USA) with a standard three-electrode glass cell, in which a Pt wire was used as the counter electrode, Ag/AgCl/KCl (saturated solution) as the reference electrode, glassy carbon electrode (GCE) modified with various catalysts as the working electrode, and KOH solution (0.1 M) as the electrolyte. The catalyst-modified working electrode was fabricated by casting an appropriate amount of catalyst ink, which was obtained by ultrasonically dispersing the catalyst (1 mg) including as-prepared N,P-GCNS, N,P-CNS, N-CNP, N-G, P-G, or commercial Pt/C (20 wt % Pt on Vulcan XC-72R) into Nafion solution (0.5 mL, 0.05 wt % in alcohol) onto the fresh surface of the GCE pretreated by hand-polishing with chamois leather containing alumina (0.05 μm) slurry. The loading amount of each catalyst was kept at 141 $\mu g\ cm^{-2}$. All of the potentials reported in this work were referenced to the reversible hydrogen electrode (RHE) scale by adding a value of 0.964 V.

ORR performance of the catalysts was investigated via cyclic voltammograms (CVs) and linear sweep voltammograms (LSVs) in either N_2 or O_2 saturated electrolyte. The scan rate was kept as 100 mV s^{-1} for CVs and 10 mV s^{-1} for LSVs tests. Oxygen reduction current was evaluated after subtracting the background capacitive current, which was tested by scanning the electrode in a N_2-saturated electrolyte at the same conditions. The electron transfer number per oxygen molecular involved in the ORR process was calculated using Koutecky−Levich (K-L) equations expressed as

$$\frac{1}{J} = \frac{1}{J_k} + \frac{1}{B\omega^{1/2}} \quad (1)$$

$$B = 0.62nFC_0D_0^{2/3}\upsilon^{-1/6} \quad (2)$$

DOI: 10.1021/acscatal.5b00601
ACS Catal. 2015, 5, 4133−4142

where J is the measured current density, J_k is the kinetic current density, B is the Levich constant, ω is the angular velocity of the rotating electrode, n is the overall number of electrons transferred in the ORR process, F is the Faraday constant (96485 C mol^{-1}), C_0 is the bulk concentration (1.2×10^{-3} mol L^{-1}) of O_2, D_0 is the diffusion coefficient (1.9×10^{-5} cm^2 s^{-1}) of O_2 in the KOH solution, and υ is the kinetic viscosity (0.01 cm^2 s^{-1}) of the electrolyte.

Rotating ring-disk electrode (RRDE) voltammograms were measured by setting the scanning rate of the disk electrode to be 10 mV s^{-1}, and the ring potential constant at 0.7 V for oxidizing the HO_2^- intermediate. The electron transfer number n and HO_2^- intermediate production percentage (HO_2^- %) were determined as

$$n = 4 \times \frac{I_d}{I_d + I_r/N} \tag{3}$$

$$HO_2^-\% = 200 \times \frac{I_r/N}{I_d + I_r/N} \tag{4}$$

where I_d is the disk current, I_r is the ring current, and N is the current collection efficiency of the Pt ring, which was determined to be 0.37. Chronoamperometric measurements were performed at a polarizing potential of 0.8 V and a rotation rate of 1600 rpm to investigate a possible poisoning effect and the stability of the catalyst. OER activity was evaluated by LSVs in the potential window ranging from 1.0 to 1.95 V versus RHE. Electrochemical impedance spectra (EIS) were recorded in the frequency range from 100 kHz to 0.01 Hz with an AC signal amplitude of 5 mV.

3. RESULTS AND DISCUSSION

3.1. Structure and Chemical Composition of the Catalysts. PANi has been deposited on various substrates (e.g., GO, graphene nanoribbons, and SBA-15 mesoporous silica) via polymerizing An in the presence of hydrochloride acid to fabricate N-doped carbon nanomaterials by carbonization.[10,16] We also noted that PA (a natural saturated cyclic acid abundant in many plant tissues) has been used as the gelator and dopant in the polymerization of An to form a porous conducting PANi hydrogel, which could be conformally coated on silicon nanoparticles through hydrogen bonding between the phosphoric acid groups in PA molecules and the SiO_2 on the Si particle surfaces.[17] Considering the large surface area of GO and the abundant oxygen-containing groups (such as hydroxyl and carboxyl) on its surface, we employed GO as the substrate and PA as the gelator/dopant for polymerization of An to implement conformal coating a layer of PANi and PA on both sides of GO nanosheets (GO@PANi/PA) through cross-link among GO, An, and PA during polymerization as illustrated in Scheme 1. Another reason for selecting PA as the dopant is that PA has been used as an activating agent to prepare activated carbon with abundant micro-/mesopores and large surface area.[18] Furthermore, our group and many other researchers have adopted phosphoric acid or phosphate as the phosphorus source for preparation of P-doped graphene or nanocarbons.[19] Therefore, we surmise that PA would act not only as a gelator during polymerization of An and formation of GO@PANi/PA hydrogel but also as an activation agent for pore-making and as the phosphorus source for P-doping during pyrolysis; thus, N- and P-codoped porous carbon conformally coated graphene nanosheets (designated N,P-GCNS) could be obtained after thermolysis of the dried GO@PANi/PA gel under nitrogen flow. As expected, the typical scanning electron microscopy (SEM) image in Figure 1a clearly shows that the as-

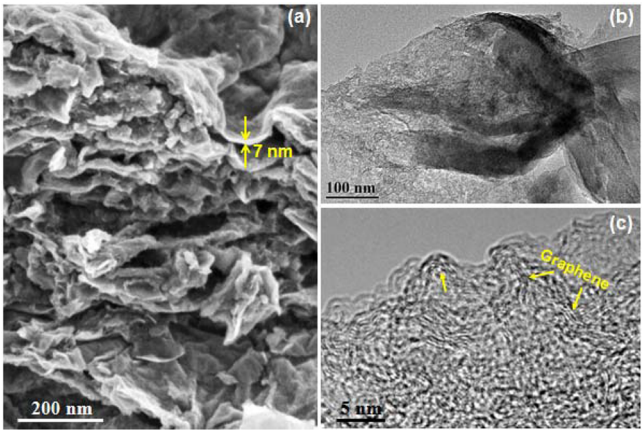

Figure 1. SEM (a) and TEM (b, c) images of N,P-GCNS.

prepared N,P-GCNS was composed of numerous crumpled sheets with thickness in the range of 5−10 nm, and ultrafine N,P-doped carbon particles converted from carbonization of PANi and PA could be observed on both sides of each sheet with uniform distribution. These wrinkled nanosheets self-assembled into a sandwich-like hierarchically porous structure. Nitrogen adsorption/desorption tests revealed that the N,P-GCNS possesses a large surface area of 900.2 m^2 g^{-1} with broad pore size distribution in the micro- and mesoranges (Figure S1, Supporting Information), which would be favorable for transportation of oxygen gas and electrolyte during oxygen electrolysis.

The porous sheet-like structure of the material was confirmed by TEM image shown in Figure 1b, and distinct corrugations could also be observed. The high-resolution TEM images in Figure 1c and Figure S2 suggest that the as-prepared N,P-GCNS had a sandwich-like structure with porous N,P-doped carbon conformal coating on few-layers-thick graphene nanosheets. This unique structure should favor electrocatalysis applications, because the active sites (i.e., N,P-doped carbon) could be almost entirely exposed to reactant molecules and the incorporated graphene nanosheets beneath the N,P-doped carbon could facilitate electron transportation during redox process, which would be beneficial for enhancement of electrocatalytic activity and electrochemical kinetics. The XRD pattern (Figure S3a) and Raman spectrum (Figure S3b) of N,P-GCNS were similar to those of the thermally reduced GO (TRG), indicating that the N,P-GCNS is carbonaceous material in nature. However, the (002) diffraction peak in the XRD pattern of N,P-GCNS was much broader and weaker than that of TRG, and the I_D/I_G ratio in the Raman spectra of the N,P-GCNS was significantly larger than that of TRG. These facts suggested that the orderly restacking of graphene nanosheets in N,P-GCNS was effectively inhibited by N,P-doped carbon, and many more defect sites were created by N and P dual-doping.[20]

The chemical composition of N,P-GCNS was evaluated by XPS. The full XPS spectrum (Figure 2a) revealed that the as-prepared N,P-GCNS consisted of C, P, N, and O, indicating both N and P atoms were doped into the material. The contents of N and P were determined to be 4.71 and 1.72 at. %,

DOI: 10.1021/acscatal.5b00601
ACS Catal. 2015, 5, 4133−4142

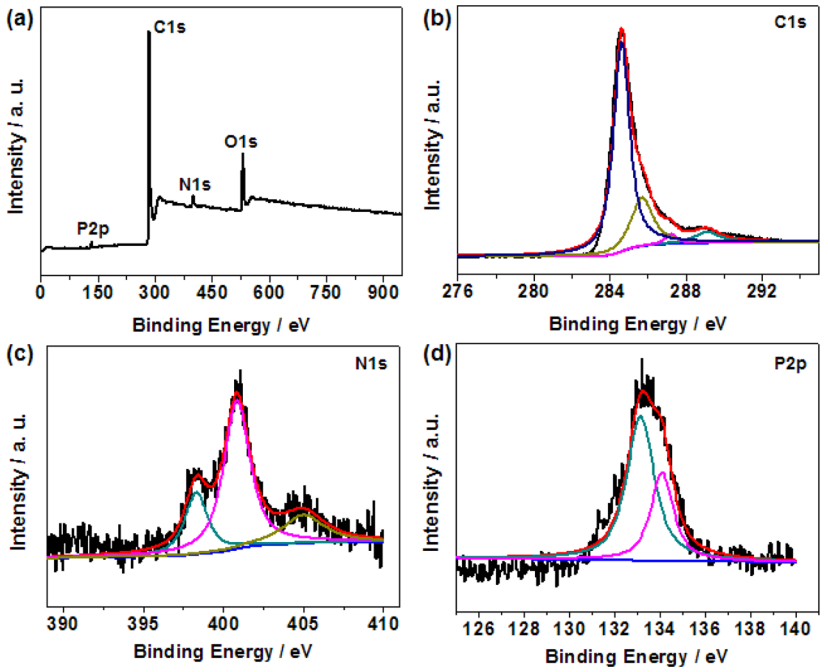

Figure 2. XPS survey spectrum (a) and the high-resolution spectra of C 1s (b), N 1s (c), and P 2p (d) of N,P-GCNS.

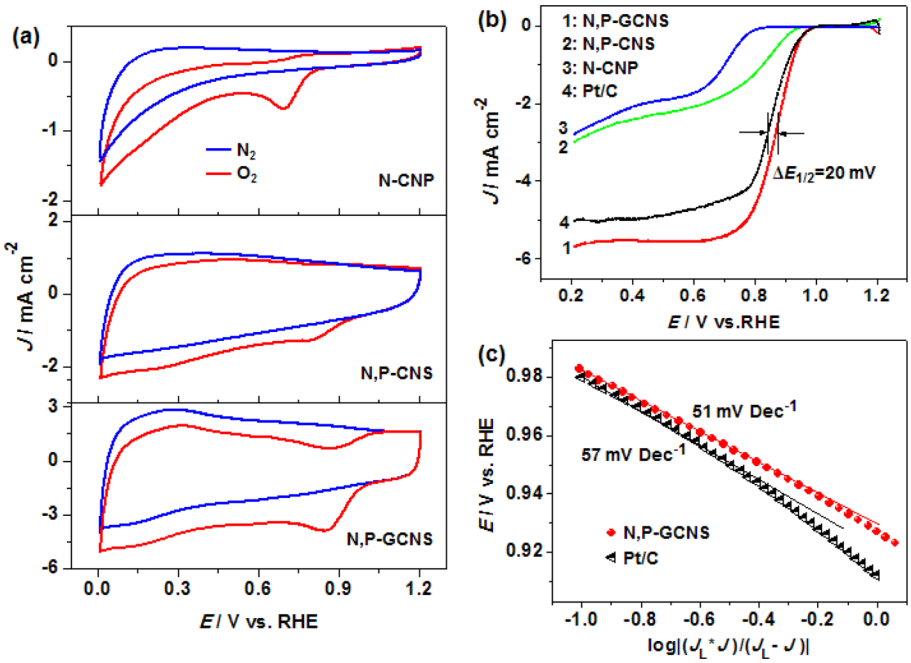

Figure 3. (a) Comparison of CV plots of N,P-GCNS, N,P-CNS, and N-CNP. (b) LSV curves of various catalysts at a rotation rate of 1600 rpm. (c) Tafel plots of ORR currents for N,P-GCNS and Pt/C.

respectively. High-resolution XPS spectra can provide more information about the bonding configuration of each component. As shown in Figure 2b, the C 1s spectrum was deconvoluted into four peaks located at 284.6, 285.7, 287.2, and 289.1 eV, which can be attributed to C═C, C—O/C═N/C—P, C═O/C—N, O—C═O, respectively.[21] The high-resolution N 1s spectra (Figure 2c) revealed that the doped N atoms existed in the form of pyridinic-N (398.3 eV), quaternary-N (400.9 eV), and chemsorbed-N (404.9 eV).[11,12] It was proposed that ORR activity of N-doped carbon materials was dependent on the content of pyridinic-N and quaternary-N, and the former improved the onset potential for ORR, whereas the latter determined the limiting current density.[22] Considering the high content of pyridinic-N and quaternary-N in the N,P-GCNS, excellent catalytic performance of the material was anticipated toward oxygen redox catalysis. The P 2p spectrum (Figure 2d) was deconvoluted into two peaks located at 133.1 and 134.1 eV, which can be ascribed to P—C and P—O bonding, respectively.[23] The peak area of the former is about 2 times that of the latter, indicating that P atoms were incorporated into the carbon framework. Additional P-doping

DOI: 10.1021/acscatal.5b00601
ACS Catal. 2015, 5, 4133−4142

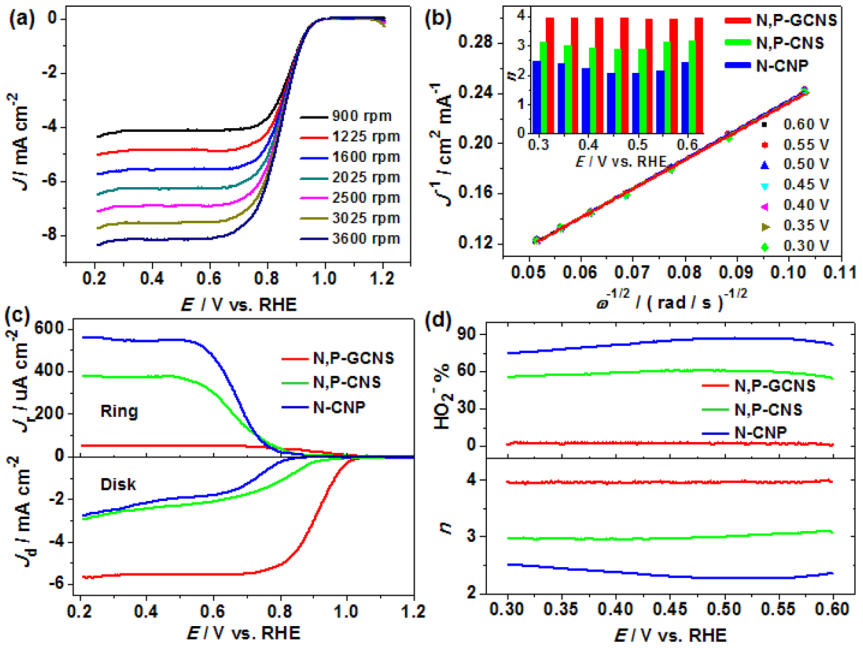

Figure 4. (a) LSV curves of N,P-GCNS at different rotating rates. (b) K-L plots of N,P-GCNS at different potentials. (Inset) Electron transfer number (n) of various catalysts at different potentials. (c) RRDE LSV curves of N,P-GCNS, N,P-CNS, and N-CNP at a rotation rate of 1600 rpm. (d) HO_2^- yields (top) during the ORR and the corresponding electron transfer number (n, bottom) of the prepared catalysts.

into N-doped carbon was found to create more active sites and trigger synergistic effects for ORR electrocatalysis.[23,24]

As mentioned above, GO acted as a structure-directing agent besides the precursor of graphene to achieve sandwich-like GO@PANi/PA, which was then converted into N,P-GCNS nanosheets with hierarchically porous structure. The template role of GO was also manifested in another two control experiments. For example, GO could direct the polymerization of An on its surface to form GO-PANi precursor, which was further evolved into sheet-like N-G (Figure S4a) upon thermolysis. In addition, PA could be absorbed on the surface of GO through hydrogen bonding, forming PA-GO precursor to finally produce sheet-like P-G (Figure S4b) after thermal treatment. In the absence of GO, each PA molecule could cross-link with more than one PANi chain via hydrogen bonding, resulting in the formation of spherical intermediate as illustrated in Figure S5a, which was finally transformed into N,P-doped carbon nanospheres (N,P-CNS) upon thermolysis (Figure S5b). The N,P-CNS exhibited much smaller surface area (411.1 $m^2 g^{-1}$) and different pore structure (Figure S6) in comparison with the N,P-GCNS. When PA was further replaced with HCl during polymerization of An, pristine PANi without PA and GO was obtained. Upon thermolysis of the pristine PANi, N-doped carbon nanoparticles (N-CNP) with irregular shape were produced (Figure S7). These facts suggested that both GO and PA played important roles in the synthesis of the porous N,P-GCNS nanosheets. Certainly, these structural differences of N,P-GCNS, N,P-CNS, and N-CNP would cause different electrocatalytic performance.

3.2. Electrocatalytic Performance of the Catalysts. ORR catalytic activity of N,P-GCNS as well as N,P-CNS and N-CNP was first investigated by means of cyclic voltammetry for comparison. As presented in Figure 3a, featureless CV plots were observed for all three samples in O_2-free KOH solution, whereas pronounced oxygen reduction peaks arose in O_2-saturated electrolyte, indicating that the three samples exhibited catalytic activity toward ORR. However, the peak potential positively shifted from 0.69 to 0.78 and 0.85 V (vs RHE) for N-CNP, N,P-CNS, and N,P-GCNS, respectively, and their corresponding oxygen reduction current density increased from 0.55 to 0.80 and 2.24 mA cm^{-2}. Evidently, the ORR activity increased in the order N-CNP, N,P-CNS, and N,P-GCNS, indicating the advantages of N and P dual-doping and the unique structure of N,P-GCNS as discussed above. Similar trends were also observed in LSV tests as shown in Figure 3b. The onset potential (E_0) increased from 0.84 V (N-CNP) to 0.95 V (N,P-CNS) and 1.01 V (N,P-GCNS). Furthermore, the corresponding oxygen reduction current density at 0.6 V increased successively from 1.70 to 2.07 and 5.56 mA cm^{-2}. Clearly, the ORR activity increased in the order N-CNP < N,P-CNS < N,P-GCNS, in good accordance with the results of CV measurements. The ORR activity of the two N,P dual-doped samples (N,P-CNS and N,P-GCNS) is much enhanced relative to that of N-CNP with only N-doping. The possible reason is that additional P-doping into N-doped carbon was reported to be able to enhance charge delocalization and asymmetric spin density of carbon atoms[25] and can also promote N-doping at the edges of graphene where electrochemical activity is high,[26] thus creating more active sites and triggering synergistic effects for ORR.[23] On the other hand, the two N,P-doped samples (i.e., N,P-CNS and N,P-GCNS) also exhibited different ORR activities. Given their N and P contents were equivalent (because only a little amount of GO was added in the preparation of N,P-GCNS while the other conditions were kept the same), their microstructures were distinctly different as discussed under section 3.1. The exposed active sites at the surface of the porous N,P-GCNS nanosheets were beneficial to full utilization by the reactants, which was similar to the case of CNT@NCNT,[12] leading to much higher activity of N,P-GCNS than that of N,P-CNS. Moreover, the incorporated graphene nanosheets in N,P-GCNS could improve its electron conductivity, and the hierarchically porous structure could

DOI: 10.1021/acscatal.5b00601
ACS Catal. 2015, 5, 4133−4142

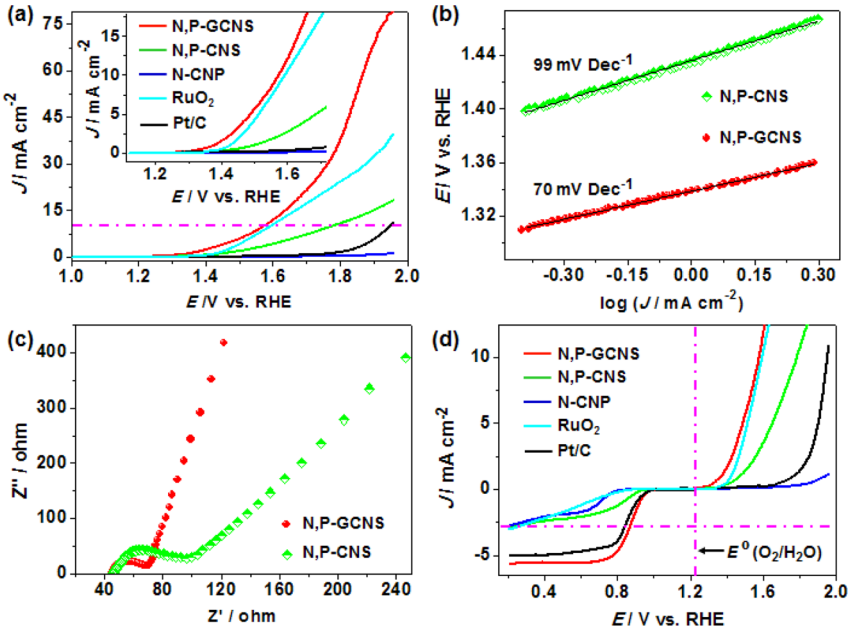

Figure 5. (a) Comparison of the OER activity of various catalysts evaluated by LSV tests at a rotation rate of 1600 rpm. (Inset) Magnified view. (b) Tafel plots of OER current for N,P-CNS and N,P-GCNS. (c) Nyquist plots of N,P-GCNS and N,P-CNS. (d) Bifunctional catalytic activity of various catalysts toward both ORR and OER.

promote O_2 and OH^- transportation, hence resulting in rapid kinetics and large cathodic current. More interestingly, the half-wave potential ($E_{1/2}$) of N,P-GCNS was 20 mV higher than that of Pt/C, and the cathodic current density of N,P-GCNS was also greater than that of Pt/C over the entire potential range, suggesting that the ORR activity of N,P-GCNS surpassed that of the benchmark Pt/C catalyst. The superior ORR-catalytic activity of N,P-GCNS to Pt/C was further confirmed by the smaller Tafel slope (51 vs 57 mV Dec^{-1}) at low overpotentials (Figure 3c).

To gain further insight into the ORR kinetics and catalytic mechanism, LSV measurements were performed at different rotating rates in the range of 900−3600 rpm, and the corresponding LSV curves are shown in Figure 4a. It can be seen that the limited diffusion current density increased with the increase of rotation rate, because the diffusion distance of the O_2-saturated electrolyte was shortened at high speeds.[27] The corresponding K-L plots are presented in Figure 4b. All of the K-L curves at different potentials are straight lines and are almost overlapped, implying first-order reaction kinetics toward the concentration of dissolved oxygen and similar electron transfer number (n) for ORR reaction at different potentials.[22] However, the LSV curves and K-L plots of N,P-CNS and N-CNP (Figure S8) were slightly different from those of N,P-GCNS, suggesting their ORR mechanisms were not exactly the same. The values of n for each catalyst at different potentials can be obtained from the slopes of the corresponding K-L curves and are plotted in the inset of Figure 4b. Clearly, the values of n changed in the ranges of 2.87−3.16 and 2.05−2.49 for N,P-CNS and N-CNP, respectively, suggesting a combined two-electron and four-electron reduction pathway with low conversion efficiency. In contrast, the values of n for N,P-GCNS at any studied potential were almost identical to 3.96, suggesting a four-electron oxygen reduction process, which is highly desired for efficient energy conversion and storage. As a result, N,P-GCNS is the most efficient ORR catalyst. This was further confirmed by RRDE tests as shown in Figure 4c. The disk current for N,P-GCNS was about 2 times higher than those for N,P-CNS and N-CNP, whereas the ring current ascribed to the oxidation of peroxide generated on the electrode was much suppressed on the N,P-GCNS electrode in comparison with those on the others. HO_2^- yield and the electron transfer number n calculated from the corresponding disk and ring current are presented in Figure 4d. Obviously, the HO_2^- yield on the N,P-GCNS electrode was below 2% in a wide range of potential, whereas the average HO_2^- yields on N,P-CNS and N-CNP electrodes were about 60 and 80%, respectively. In addition, the n value for the N,P-GCNS electrode was much higher than those for the other two electrodes, in good agreement with the results obtained from the K-L plots.

To further investigate the potential application of N,P-GCNS as a bifunctional catalyst for oxygen electrocatalysis, OER activity of N,P-GCNS as well as other catalysts was evaluated by sweeping the RDE potential from 1.0 to 1.95 V, and the corresponding LSV curves are plotted in Figure 5a. It can be seen that the OER onset potentials were 1.32, 1.39, 1.41, 1.67, and 1.78 V for N,P-GCNS, RuO_2, N,P-CNS, Pt/C, and N-CNP, respectively. The OER current density at any selected potential always decreased in this order. For example, the current densities at 1.9 V were 70.75, 32.41, 15.57, 6.50, and 0.78 mA cm^{-2} for N,P-GCNS, RuO_2, N,P-CNS, Pt/C, and N-CNP, respectively. Therefore, N,P-GCNS exhibited the earliest onset potential and the greatest current density among the studied catalysts, indicating that the OER activity of N,P-GCNS was the highest among the carbon-based catalysts and was even higher than that of RuO_2 (one of the best OER catalysts at present). Usually, the OER activity of a material is judged by the potential required to oxidize water at a current density of 10 mA cm^{-2}, which is a metric relevant to solar fuel synthesis.[28,29] In our case, the potentials corresponding to the current density of 10 mA cm^{-2} (denoted E_{J10}) for N,P-GCNS, RuO_2, N,P-CNS, Pt/C, and N-CNP were 1.57, 1.59, 1.79, 1.94, and >2 V, respectively. Despite the fact that Pt/C showed higher ORR

DOI: 10.1021/acscatal.5b00601
ACS Catal. 2015, 5, 4133−4142

Table 1. Comparison of the Bifunctional Catalytic Activity of N,P-GCNS with Other Electrocatalysts

catalyst	$E_{onset,ORR}$ (V)	E_{ORR} (V) (−3 mA cm^{-2})	E_{OER} (V) (10 mA cm^{-2})	ΔE (V) ($E_{OER} - E_{ORR}$)	ref
NGSH	0.88	0.70	1.63	0.93	11
N/C	0.99	0.63	1.76	1.06	12
20% Pt/C		0.86	2.02	1.16	29
20% Ru/C		0.61	1.62	1.01	29
20% Ir/C		0.69	1.61	0.92	29
MnO_x		0.73	1.77	1.04	29
N-graphene/CNT	0.88	0.69	1.65	0.96	32
PCN-CFP	0.94	0.72	1.63	0.91	33
Co/N-C-800	0.83	0.74	1.60	0.86	34
CCH-2/C	0.93	0.82	1.74	0.92	35
Co_3O_4/N-rmGO	0.88	0.85	1.54	0.69	36
$NiCo_2S_4$@N/S-rGO	0.85	0.72	1.70	0.98	37
$NiCo_2O_4$/G	0.89	0.56	1.69	1.13	38
Co_3O_4/2.7Co_2MnO_4	0.90	0.68	1.77	1.09	39
NCO-A_1	0.93	0.78	1.62	0.84	40
Co/N-C-800		0.74	1.60	0.86	41
Pt/C to BSCF/C = 4:1	0.88	0.81	1.61	0.80	42
N,P-GCNS	1.01	0.86	1.57	0.71	this work

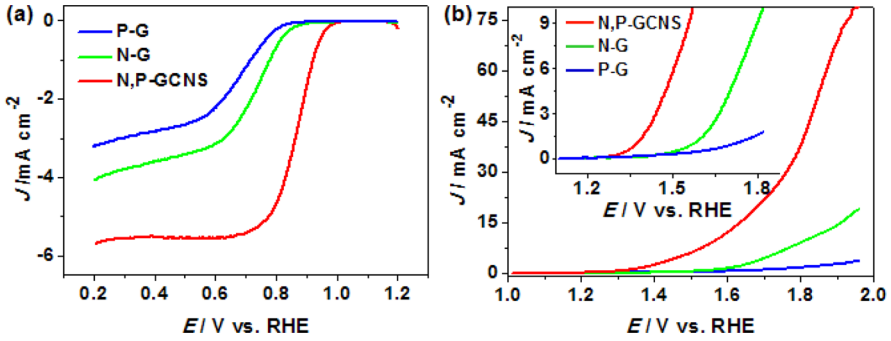

Figure 6. ORR (a) and OER (b) LSV plots of graphene-based catalysts with sheet-like morphology and different heteroatom doping, illustrating the synergetic effect of N,P dual-doping on oxygen electrocatalysis performance.

activity than N,P-CNS, its OER activity was inferior to that of N,P-CNS and much worse than that of N,P-GCNS. According to the criterion of E_{J10}, N,P-GCNS not only is the best OER catalyst among the carbon-based ones studied in this work but also has better activity than RuO_2 (1.59 V), N-doped carbon (N/C, 1.61 V), and IrO_2/C (1.60 V).[30] It is worth noting that the order of OER activity for the three metal-free samples resembled the trend of ORR activity. The facts above gave us three inspirations at least: (1) N,P-GCNS can be used as an efficient bifunctional electrocatalyst to reversibly catalyze the reversible interconversion between O_2 and OH^- (i.e., $O_2 + 4e^- + 2H_2O \Leftrightarrow 4OH^-$) in alkaline, although the detailed catalytic mechanism is unclear at present; (2) multiple-element doping (e.g., N and P in our case) is better than single-element doping for improving the activity of OER due to the synergetic effects similar to those observed in ORR electrocatalysis;[31] (3) engineering the microstructure of the catalyst is of paramount importance for enhancing its catalytic kinetics. Taking the two N,P-doping samples (i.e., N,P-GCNS and N,P-CNS) as an example, N,P-CNS consisted of large sub-microspheres with small surface area (Figures S5 and S6); only a small part of the active sites was exposed to the reactants. Whereas N,P-GCNS was composed of ultrathin nanosheets with hierarchal porous structure and large surface area (Figure 1 and Figure S1), its active sites were mainly concentrated on the surface of the porous nanosheets and were thus propitious to full utilization by the reactants. In addition, the incorporated crystalline graphene nanosheets beneath the layer of doped carbon could significantly improve the conductivity of the material. Accordingly, N,P-GCNS exhibited a smaller OER Tafel slope (Figure 5b), a smaller diameter of the semicircle in the Nyquist plots (Figure 5c), and thus a much smaller charge transfer resistance and better kinetics than N,P-CNS.

The bifunctional catalytic ability of various catalysts toward both ORR and OER is further compared in Figure 5d in a wide range of potential. Obviously, N,P-GCNS exhibited the smallest overpotential and the highest activity toward both ORR and OER among these catalysts. Because current density is of practical importance for electrochemical and photoelectrochemical applications, the bifunctional catalytic activity is usually evaluated by the difference in potential between the OER current density at 10 mA cm^{-2} and the ORR current density at −3 mA cm^{-2} according to the equation $\Delta E = E_{J10,OER} - E_{J-3,ORR}$. A smaller ΔE value means better bifunctional catalytic activity and more potential for practical applications of the catalyst. Among the studied catalysts, N,P-GCNS exhibited the most negative $E_{J10,OER}$, the most positive $E_{J-3,ORR}$, and hence the smallest ΔE with a value of 0.71 V. The main parameters of some reported bifunctional electrocatalysts are listed in Table 1 for comparison.[32−42] Clearly, N,P-GCNS is among the best bifunctional oxygen electrode catalysts, showing great promise

DOI: 10.1021/acscatal.5b00601
ACS Catal. 2015, 5, 4133−4142

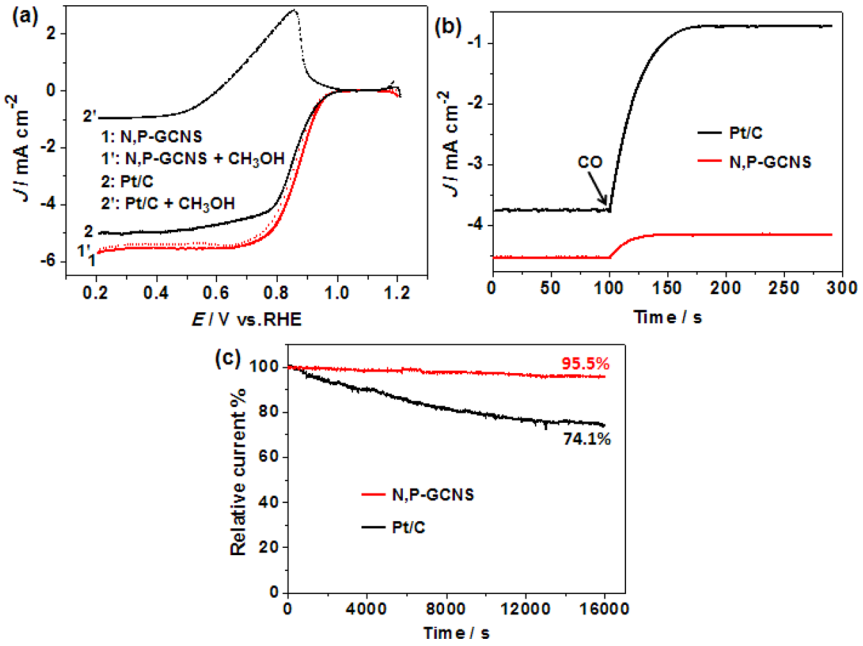

Figure 7. (a) Methanol crossover tests performed on RDE with a rotation rate of 1600 rpm by injecting methanol into the electrolyte to reach a concentration of 3 mol L^{-1}. (b) CO poisoning tests by introducing additional CO into the electrolyte. (c) Comparison of the stabilities of N,P-GCNS and Pt/C.

in the fields of rechargeable metal−air batteries and unitized regenerative fuel cells (URFC).

The above experimental data reveal that heteroatom doping, incorporation of graphene, and microstructure have important influence on oxygen electrocatalysis performances of carbon-based electrocatalysts (e.g., N-CNP, N,P-CNS, and N,P-GCNS). To illustrate the synergetic effect of N and P dual-doping on the electrocatalytic activity of doped nanocarbons more clearly, we further compared the ORR and OER activities of a series of sheet-like graphene-based materials including N-G, P-G, and N,P-GCNS with N or P single-doping and N,P dual-doping, respectively. Their ORR and OER LSV plots are provided in Figure 6, panels a and b, respectively. The corresponding catalytic performance parameters are listed in Table S1. It is clear that the N,P-GCNS exhibited much higher catalytic activity than either N-G or P-G toward ORR and OER, illustrating the advantage of N,P dual-doping over N or P single-doping due to the synergetic effects as intensively investigated in the literature about ORR performance enhanced by multiple-heteroatom doping.[14,25]

Fuel crossover effect, CO poisoning, and stability are important issues challenging the cathode materials in current fuel cell techniques.[43,44] First, possible methanol crossover effect on N,P-GCNS was investigated by LSV tests, and the results are compared with those of Pt/C in Figure 7a. When methanol was injected, the reduction of oxygen was totally depressed by oxidization of methanol on Pt/C, suggesting poor tolerance of Pt/C to methanol. In contrast, no conspicuous change was observed on the LSV curves of N,P-GCNS, indicating excellent tolerance of N,P-GCNS to methanol crossover. Then, CO poisoning tests were performed by current−time (i−t) chronoamperometry. As shown in Figure 7b, a significant decrease in current density was observed on Pt/C when additional CO was introduced into the electrolyte due to deactivation of the catalyst, whereas only a very slight variation occurred on the N,P-GCNS electrode, which was caused by the decrease of the oxygen partial pressure owing to introduction of CO. As a result, N,P-GCNS exhibited much better resistance to CO poisoning than Pt/C. Finally, the durability of the catalysts was tested by continuous chronoamperometric measurements. After testing for 16000 s under the same conditions, a slight performance attenuation (4.5%) was observed for N,P-GCNS as shown in Figure 7c, whereas the catalytic activity of Pt/C significantly degraded with a sharp current loss (25.9%) due to the surface oxidization and particle dissolution/aggregation over time, which is a common failing of metal-based electrocatalysts. These results highlighted the advantage of the metal-free N,P-GCNS over other metal-based electrocatalysts.

4. CONCLUSIONS

In summary, we have successfully prepared N,P-GCNS nanosheets with hierarchically porous sandwich-like structure by direct pyrolysis of a polymer gel composed of GO, PANi, and PA. This strategy is simple and cost-effective for mass production of metal-free multiple-element-doped nanocarbons. Furthermore, N,P-GCNS exhibited superb bifunctional catalytic activity toward both ORR and OER with exceptionally low overpotential, high catalytic current density, excellent tolerance to methanol crossover, good resistance to CO poisoning, and long-term durability, hence holding promise for applications in rechargeable metal−air batteries and URFCs. It was found that (1) multiple-element-doped nanocarbons exhibited much better bifunctional catalytic activity than single-doped ones due to the synergetic effects; (2) the more active sites exposed to the reactants, the better catalytic activity the catalyst would show; (3) the large active surface area and the hierarchical pores ensured the accessibility of the reactant molecules and rapid mass transportation; and (4) the integrated crystalline graphene nanosheets could promote charge transfer during the redox process.

DOI: 10.1021/acscatal.5b00601
ACS Catal. 2015, 5, 4133−4142

■ ASSOCIATED CONTENT

Supporting Information

The Supporting Information is available free of charge on the ACS Publications website at DOI: 10.1021/acscatal.5b00601.

Additional structural characterizations and electrochemical measurements (PDF)

■ AUTHOR INFORMATION

Corresponding Authors

*(Z.W.) E-mail: zdwei@cqu.edu.cn.
*(X.G.) E-mail: gouxlr@126.com.

Notes

The authors declare no competing financial interest.

■ ACKNOWLEDGMENTS

This work was supported financially by the China National 973 Program (2012CB720300 and 2012CB215500), by the NSFC of China (21436003, 21176271, and 51071131), and by Education Department of Sichuan Province (rs2013, 13ZA0014, and 15TD0018).

■ REFERENCES

(1) (a) Katsounaros, I.; Cherevko, S.; Zeradjanin, A. R.; Mayrhofer, K. J. J. *Angew. Chem., Int. Ed.* **2014**, *53*, 102−121. (b) Shao, Y.; Park, S.; Xiao, J.; Zhang, J.; Wang, Y.; Liu, J. *ACS Catal.* **2012**, *2*, 844−857. (c) Walter, M. G. E.; Warren, L.; McKone, J. R.; Boettcher, S. W.; Mi, Q.; Santori, E. A.; Lewis, N. S. *Chem. Rev.* **2010**, *110*, 6446−6473.

(2) (a) Chen, S.; Duan, J.; Jaroniec, M.; Qiao, S. Z. *Adv. Mater.* **2014**, *26*, 2925−2930. (b) Debe, M. K. *Nature* **2012**, *486*, 43−51.

(3) (a) McCrory, C. C. L.; Jung, S.; Peters, J. C.; Jaramillo, T. F. *J. Am. Chem. Soc.* **2013**, *135*, 16977−16987. (b) Reier, T.; Oezaslan, M.; Strasser, P. *ACS Catal.* **2012**, *2*, 1765−1772. (c) Mayrhofer, K. J. J.; Arenz, M. *Nat. Chem.* **2009**, *1*, 518−519.

(4) (a) Menezes, P. W.; Indra, A.; González-Flores, D.; Sahraie, N. R.; Zaharieva, I.; Schwarze, M.; Strasser, P.; Dau, H.; Driess, M. *ACS Catal.* **2015**, *5*, 2017−2027. (b) Hou, Y.; Wen, Z.; Cui, S.; Ci, S.; Mao, S.; Chen, J. H. *Adv. Funct. Mater.* **2015**, *25*, 872−882.

(5) (a) Shen, M.; Ruan, C.; Chen, Y.; Jiang, C. H.; Ai, K.; Lu, L. H. *ACS Appl. Mater. Interfaces* **2015**, *7*, 1207−1218. (b) Jung, J.; Jeong, H. Y.; Lee, J. S.; Kim, M. G.; Cho, J. *Angew. Chem., Int. Ed.* **2014**, *53*, 4582−4586. (c) Jung, K.; Hwang, S. M.; Park, M. S.; Kim, K. J.; Kim, J. G.; Dou, S. X.; Kim, J. H.; Lee, J. W. *Sci. Rep.* **2014**, *5*, 7665. (d) Cheng, F.; Shen, J.; Peng, B.; Pan, Y.; Tao, Z.; Chen, J. *Nat. Chem.* **2011**, *3*, 79−84.

(6) (a) Gong, K.; Du, F.; Xia, Z.; Durstock, M.; Dai, L. M. *Science* **2009**, *323*, 760−764. (b) Yang, L.; Jiang, S.; Zhao, Y.; Zhu, L.; Chen, S.; Wang, X.; Wu, Q.; Ma, J.; Ma, Y.; Hu, Z. *Angew. Chem., Int. Ed.* **2011**, *50*, 7132−7135. (c) Liu, Z. W.; Peng, F.; Wang, H. J.; Yu, H.; Zheng, W. X.; Yang, J. *Angew. Chem., Int. Ed.* **2011**, *50*, 3257−3261.

(7) (a) Ding, W.; Wei, Z. D.; Chen, S.; Qi, X.; Yang, T.; Hu, J.; Wang, D.; Wan, L. J.; Alvi, S. F.; Li, L. *Angew. Chem., Int. Ed.* **2013**, *52*, 11755−11759. (b) Yao, Z.; Nie, H.; Yang, Z.; Zhou, X.; Liu, Z.; Huang, S. *Chem. Commun.* **2012**, *48*, 1027−1029. (c) Yang, Z.; Yao, Z.; Li, G.; Fang, G.; Nie, H.; Liu, Z.; Zhou, X.; Chen, X.; Huang, S. *ACS Nano* **2012**, *6*, 205−211.

(8) (a) Jeon, I.; Zhang, S.; Zhang, L.; Choi, H.; Seo, J.; Xia, Z.; Dai, L.; Baek, J. *Adv. Mater.* **2013**, *25*, 6138−6145. (b) Cheon, J. Y.; Kim, J. H.; Kim, J. H.; Goddeti, K. C.; Park, J. Y.; Joo, S. H. *J. Am. Chem. Soc.* **2014**, *136*, 8875−8878.

(9) Cheng, Y.; Xu, C.; Jia, L.; Gale, J. D.; Zhang, L.; Liu, C.; Shen, P. K.; Jiang, S. P. *Appl. Catal., B* **2015**, *163*, 96−104.

(10) Lin, Z.; Waller, G. H.; Liu, Y.; Liu, M.; Wong, C. P. *Carbon* **2013**, *53*, 130−136.

(11) Tian, G. L.; Zhao, M. Q.; Yu, D.; Kong, X. Y.; Huang, J. Q.; Zhang, Q.; Wei, F. *Small* **2014**, *10*, 2251−2259.

(12) Tian, G. L.; Zhang, T. Q.; Zhang, B.; Jin, Y. G.; Huang, J. Q.; Su, D. S.; Wei, F. *Adv. Funct. Mater.* **2014**, *24*, 5956−5961.

(13) (a) Gong, X.; Liu, S.; Ouyang, C.; Strasser, P.; Yang, R. *ACS Catal.* **2015**, *5*, 920−927. (b) Choi, C. H.; Chung, M. W.; Park, S. H.; Woo, S. I. *Phys. Chem. Chem. Phys.* **2013**, *15*, 1802−1805. (c) Choi, C. H.; Chuang, M. W.; Kwon, H. C.; Park, S. H.; Woo, S. I. *J. Mater. Chem. A* **2013**, *1*, 3694−3699.

(14) Zhang, J. T.; Zhao, Z. H.; Xia, Z. H.; Dai, L. M. *Nat. Nanotechnol.* DOI: 10.1038/NNANO.2015.48.

(15) Zhang, Q.; Li, R.; Zhang, M.; Zhang, B.; Gou, X. *Electrochim. Acta* **2014**, *115*, 425−433.

(16) (a) Liu, M.; Song, Y.; He, S.; Tjiu, W. W.; Pan, J.; Xia, Y. Y. *ACS Appl. Mater. Interfaces* **2014**, *6*, 4214−4222. (b) Silva, R.; Voiry, D.; Chhowalla, M.; Asefa, T. *J. Am. Chem. Soc.* **2013**, *135*, 7823−7826.

(17) (a) Pan, L.; Yu, G.; Zhai, D.; Lee, H. R.; Zhao, W.; Liu, N.; Wang, H.; Tee, B. C.-K.; Shi, Y.; Cui, Y.; Z. Bao, N. *Proc. Natl. Acad. Sci. U. S. A.* **2012**, *109*, 9287−9292. (b) Wu, H.; Yu, G.; Pan, L.; Liu, N.; McDowell, M. T.; Bao, Z. N.; Cui, Y. *Nat. Commun.* **2013**, *4*, 1943−1948.

(18) Cheng, C.; Zhang, J.; Mu, Y.; Gao, J.; Feng, Y.; Liu, H.; Guo, Z.; Zhang, C. *J. Anal. Appl. Pyrolysis* **2014**, *108*, 41−46.

(19) (a) Li, R.; Wei, Z. D.; Gou, X. L.; Xu, W. *RSC Adv.* **2013**, *3*, 9978. (b) Sánchez, M. L.; Primo, A.; García, H. *Angew. Chem., Int. Ed.* **2013**, *52*, 11813−11816.

(20) Wen, Z.; Wang, X.; Mao, S.; Bo, Z.; Kim, H.; Cui, S.; Lu, G.; Feng, X.; Chen, J. *Adv. Mater.* **2012**, *24*, 5610−5616.

(21) Lin, Z.; Waller, G.; Liu, Y.; Liu, M.; Wong, C. P. *Adv. Energy Mater.* **2012**, *2*, 884−888.

(22) Lai, L.; Potts, J. R.; Zhan, D.; Wang, L.; Poh, C. K.; Tang, C.; Gong, H.; Shen, Z.; Lin, J.; Ruoff, R. S. *Energy Environ. Sci.* **2012**, *5*, 7936−7942.

(23) Yang, D. S.; Bhattacharjya, D.; Inamdar, S.; Park, J.; Yu, J. S. *J. Am. Chem. Soc.* **2012**, *134*, 16127−16130.

(24) Jiang, H. L.; Zhu, Y. H.; Feng, Q.; Su, Y. H.; Yang, X. L.; Li, C. Z. *Chem. - Eur. J.* **2014**, *20*, 3106−3112.

(25) Choi, C. H.; Park, S. H.; Woo, S. I. *ACS Nano* **2012**, *6*, 7084−7091.

(26) Wang, X.; Li, X.; Zhang, L.; Weber, P. K.; Wang, H.; Guo, J.; Dai, H. J. *Science* **2009**, *324*, 768−771.

(27) Zhang, Y.; Chu, M.; Yang, L.; Deng, W.; Pan, Y.; Ma, M.; Xie, Q. *Chem. Commun.* **2014**, *50*, 6382−6385.

(28) Deng, X.; Tüysüz, H. *ACS Catal.* **2014**, *4*, 3701−3714.

(29) Gorlin, Y.; Jaramillo, T. F. *J. Am. Chem. Soc.* **2010**, *132*, 13612−13614.

(30) Zhao, Y.; Nakamura, R.; Kamiya, K.; Nakanishi, S.; Hashimoto, K. *Nat. Commun.* **2013**, *4*, 2390−2396.

(31) Higgins, D.; Hoque, M. A.; Hassan, F.; Choi, J.; Kim, B.; Chen, Z. *ACS Catal.* **2014**, *4*, 2734−2740.

(32) Wen, Z. H.; Ci, S. Q.; Hou, Y.; Chen, J. H. *Angew. Chem., Int. Ed.* **2014**, *53*, 6496−6500.

(33) Ma, T.; Ran, J.; Dai, S.; Jaroniec, M.; Qiao, S. Z. *Angew. Chem., Int. Ed.* **2015**, *54*, 4646−4650.

(34) Su, Y. H.; Zhu, Y. H.; Jiang, H. L.; Shen, J. H.; Yang, X. L.; Zou, W. J.; Chen, J. D.; Li, C. Z. *Nanoscale* **2014**, *6*, 15080−15089.

(35) Wang, Y.; Ding, W.; Chen, S.; Nie, W.; Xiong, K.; Wei, Z. D. *Chem. Commun.* **2014**, *50*, 15529−15532.

(36) Liang, Y.; Li, Y.; Wang, H.; Zhou, J.; Wang, J.; Regier, T.; Dai, H. J. *Nat. Mater.* **2011**, *10*, 780−786.

(37) Liu, Q.; Jin, J. T.; Zhang, J. Y. *ACS Appl. Mater. Interfaces* **2013**, *5*, 5002−5008.

(38) Lee, D. U.; Kim, B. J.; Chen, Z. W. *J. Mater. Chem. A* **2013**, *1*, 4754−4762.

(39) Wang, D. D.; Chen, X.; Evans, D. G.; Yang, W. S. *Nanoscale* **2013**, *5*, 5312−5315.

(40) Prabu, M.; Ketpang, K.; Shanmugam, S. *Nanoscale* **2014**, *6*, 3173−3181.

(41) Su, Y.; Zhu, Y.; Jiang, H.; Shen, J.; Yang, X.; Zou, W.; Chen, J.; Li, C. *Nanoscale* **2014**, *6*, 15080−15089.

DOI: 10.1021/acscatal.5b00601
ACS Catal. 2015, 5, 4133−4142

(42) Zhu, Y.; Su, C.; Xu, X.; Zhou, W.; Ran, R.; Shao, Z. *Chem. - Eur. J.* **2014**, *20*, 15533−15542.
(43) Jin, J.; Pan, F.; Jiang, L.; Fu, X.; Liang, A.; Wei, Z.; Zhang, J.; Sun, G. *ACS Nano* **2014**, *8*, 3313−3321.
(44) Yu, D.; Xue, Y.; Dai, L. *J. Phys. Chem. Lett.* **2012**, *3*, 2863−2870.

DOI: 10.1021/acscatal.5b00601
ACS Catal. 2015, 5, 4133−4142